IOP PUBLISHING PHYSICS IN MEDICINE AND BIOLOGY

Phys. Med. Biol. 52 (2007) 1893–1908 doi:10.1088/0031-9155/52/7/009

Separation of input function for rapid measurement of quantitative $CMRO_2$ and CBF in a single PET scan with a dual tracer administration method

Nobuyuki Kudomi, Hiroshi Watabe, Takuya Hayashi and Hidehiro Iida

Department of Investigative Radiology, Advanced Medical-Engineering Center, National Cardiovascular Center-Research Institute, 5-7-1, Fujishirodai, Suita, Osaka 565-8565, Japan

E-mail: kudomi@ri.ncvc.go.jp

Received 1 September 2006, in final form 3 January 2007
Published 12 March 2007
Online at stacks.iop.org/PMB/52/1893

Abstract

Cerebral metabolic rate of oxygen ($CMRO_2$), oxygen extraction fraction (OEF) and cerebral blood flow (CBF) images can be quantified using positron emission tomography (PET) by administrating ^{15}O-labelled water ($H_2^{15}O$) and oxygen ($^{15}O_2$). Conventionally, those images are measured with separate scans for three tracers $C^{15}O$ for CBV, $H_2^{15}O$ for CBF and $^{15}O_2$ for $CMRO_2$, and there are additional waiting times between the scans in order to minimize the influence of the radioactivity from the previous tracers, which results in a relatively long study period. We have proposed a dual tracer autoradiographic (DARG) approach (Kudomi *et al* 2005), which enabled us to measure CBF, OEF and $CMRO_2$ rapidly by sequentially administrating $H_2^{15}O$ and $^{15}O_2$ within a short time. Because quantitative CBF and $CMRO_2$ values are sensitive to arterial input function, it is necessary to obtain accurate input function and a drawback of this approach is to require separation of the measured arterial blood time–activity curve (TAC) into pure water and oxygen input functions under the existence of residual radioactivity from the first injected tracer. For this separation, frequent manual sampling was required. The present paper describes two calculation methods: namely a linear and a model-based method, to separate the measured arterial TAC into its water and oxygen components. In order to validate these methods, we first generated a blood TAC for the DARG approach by combining the water and oxygen input functions obtained in a series of PET studies on normal human subjects. The combined data were then separated into water and oxygen components by the present methods. CBF and $CMRO_2$ were calculated using those separated input functions and tissue TAC. The quantitative accuracy in the CBF and $CMRO_2$ values by the DARG approach did not exceed the acceptable range, i.e., errors in those values were within 5%, when the area under the curve in the input function of the second tracer was larger than half of the first one. Bias and deviation in those values were also compatible to that of the conventional method, when noise

0031-9155/07/071893+16$30.00

was imposed on the arterial TAC. We concluded that the present calculation based methods could be of use for quantitatively calculating CBF and $CMRO_2$ with the DARG approach.

1. Introduction

Cerebral metabolic rate of oxygen ($CMRO_2$), oxygen extraction fraction (OEF) and cerebral blood flow (CBF) images have enabled us to understand the pathophysiological basis of cerebrovascular disorders. Positron emission tomography (PET) allows us to quantitatively measure the CBF and $CMRO_2$. These measurements can be achieved using a protocol involving separate PET scans, one after the administration of each of three distinct ^{15}O-labelled radioactive tracers: $H_2{}^{15}O$ or $C^{15}O_2$ for CBF, $^{15}O_2$ for $CMRO_2$, and $C^{15}O$ for cerebral blood volume (CBV) (Frackowiack *et al* 1980a, 1980b, Mintun *et al* 1984, Lammertsma and Jones 1983). However, the complex procedure and its relatively long protocol often limit its applicability and also make it difficult to perform at different physiological conditions.

Quantitative images of CBF and $CMRO_2$ by PET are calculated on the basis of a single-tissue compartment model of oxygen and water kinetics (Frackowiack *et al* 1980a, 1980b, Mintun *et al* 1984, Lammertsma and Jones 1983). The steady-state method (Subramanyam *et al* 1978, Lammertsma *et al* 1982, Correia *et al* 1985, Okazawa *et al* 2001a, 2001b) has been employed in a number of studies in which quantitative images are estimated from data acquired while in the steady state reached during continuous inhalation of $C^{15}O_2$ and $^{15}O_2$. This method can be employed using a simple procedure and mathematical formula, but has several limitations. A prolonged data-acquisition period (approximately 1 h) is required, and the procedure is sensitive to error sources such as statistical noise and tissue heterogeneity (Lammertsma *et al* 1982, Correia *et al* 1985). An additional drawback is the relatively high level of radiation exposure required to reach the steady state.

An alternative autoradiographic method (ARG) using only short administration times for each of the three tracers, i.e., the three-step autoradiographic method (3SARG) has been developed (Mintun *et al* 1984) and subsequently simplified and optimized (Iida *et al* 1993, Sadato *et al* 1993, Hatazawa *et al* 1995, Shidahara *et al* 2002, Hattori *et al* 2004). CBF images can be obtained by a $H_2{}^{15}O$ autoradiographic method, using a PET counts-versus-CBF nomogram, which follows a simple look-up table procedure (Raichle *et al* 1983, Herscovich *et al* 1983, Kanno *et al* 1987); the quantitative accuracy of these images is improved when influence of input delay, which is the time difference between brain input function and detector device, and dispersion, which is caused by flow speed difference of liquid in a catheter tube due to viscosity, are corrected (Iida *et al* 1986, 1988). $CMRO_2$ and the oxygen extraction fraction (OEF) can be estimated using data acquired during $^{15}O_2$ inhalation, but must be corrected for clearance of radioactivity associated with CBF (Mintun *et al* 1984), CBV and the level of recirculating radioactive water (Iida *et al* 1993). Although the total time required for 3SARG is less than that of the steady-state method, it still requires at least half an hour, with waiting times between the scans to reduce the radioactivity of the tracer administered previously.

There have been other attempts to obtain CBF and $CMRO_2$ images more rapidly (Huang *et al* 1986, Holden *et al* 1988, Meyer *et al* 1987, Ohta *et al* 1992, Ho and Feng 1999). Mathematical refinement has allowed images to be generated from data from a single scan alone upon a bolus inhalation of $^{15}O_2$. The quality of the image suffers, however, from statistical noise due to the lack of predictability of the multiple parameters of CBF, $CMRO_2$, and the arterial vascular compartment (V_0) and the limited acquisition time (Meyer *et al* 1987, Ohta *et al* 1992). Therefore, this technique has not been generally applied in clinical settings,

but has been used primarily for research purposes (Fujita *et al* 1999, Vafaee and Gjedde 2000, Okazawa *et al* 2001a, 2001b, Mintun *et al* 2002).

Recently, rapid CBF and $CMRO_2$ measurement was achieved by administration of dual tracers during a single PET scan and the use of an integration method, i.e., dual tracer autoradiographic (DARG) approach (Kudomi *et al* 2005). This approach can shorten the total study period for both CBF and $CMRO_2$ measurement as compared to the 3SARG approach. It is thus expected to serve as a tool for faster or repeated assessment of flow and metabolism during multiple physiological or pathological conditions while maintaining the image quality and quantitative accuracy.

The DARG protocol was typically implemented in a short time interval of 3 min in a single PET scan conducted during the sequential administration of $H_2^{15}O$ and $^{15}O_2$. A mathematical formula based on the integration method was derived to calculate the values of CBF, OEF and $CMRO_2$ from the PET scan data, and was applicable to the data obtained after the administration of tracers in either order, i.e. $H_2^{15}O$ injection followed by $^{15}O_2$ inhalation ($H_2^{15}O$–$^{15}O_2$) or $^{15}O_2$ inhalation followed by $H_2^{15}O$ injection ($^{15}O_2$–$H_2^{15}O$). In the formula, the radioactivity concentrations in the artery, i.e. arterial input functions for the ^{15}O-labelled oxygen and ^{15}O-labelled water must be provided in order to compute the quantitative CBF and $CMRO_2$ values.

The arterial input function of whole blood including oxygen and water is usually obtained from a continuously measured arterial blood time–activity curve (TAC) by a beta-ray detector (Kanno *et al* 1987, Iida *et al* 1986) or coincidence detector (Eriksson *et al* 1988, Eriksson and Kanno 1991, Votaw *et al* 1998, Kudomi *et al* 2003). In the DARG approach, it is necessary to separate the $^{15}O_2$ and $H_2^{15}O$ contents in the arterial TAC during the second phase of the scan because the arterial blood contains not only the radioactivity of the second tracer but also the residual activity of the first tracer. Thus, the radioactivity in the arterial blood during the second phase of the scan is always the summation of the radioactivity from $^{15}O_2$ and $H_2^{15}O$. Moreover, after its administration, $^{15}O_2$ coexists in arterial blood with labelled or recirculating $H_2^{15}O$, which is a metabolite. A modelling approach (Iida *et al* 1993) enables us to predict the TAC of the recirculating water, but this approach is based on an assumption that there is no radioactivity in the arterial blood at the time of $^{15}O_2$ administration and it cannot be applied when residual radioactivity of $H_2^{15}O$ exists in the arterial blood. Instead of using the modelling approach, Kudomi *et al* (2005) performed frequent manual sampling of arterial blood and centrifugation to separate plasma from whole blood in order to predict the recirculating water content in the whole blood. However, this procedure is labour intensive and hampers the clinical application of the DARG protocol.

In this paper, we have proposed two methods: (A) a linear method and (B) a model-based method to separate the $^{15}O_2$ and $H_2^{15}O$ contents from a measured arterial TAC in which both $^{15}O_2$ and $H_2^{15}O$ coexisted for the DARG approach. By these methods, no manual sampling of arterial blood is required to separate the $^{15}O_2$ and $H_2^{15}O$ contents. In order to evaluate the proposed methods, simulation studies were performed.

2. Materials and methods

2.1. Separation methods

In this section, we described two separation methods. In both methods, the separation procedure from measured whole blood TAC ($A_t(t)$) to input functions of pure $H_2^{15}O$ ($F_w(t)$) and $^{15}O_2$ ($F_o(t)$) consists of two parts, one is to account for residual activity for the first tracer

during the second phase, and the other is to account for the metabolic product of $^{15}O_2$, i.e., recirculating water.

(A) Linear method. For the $H_2^{15}O$–$^{15}O_2$ protocol, we first estimated the TAC for the residual radioactivity from the first tracer ($H_2^{15}O$) remaining during the second phase by extrapolating the combined TAC in the first phase by the following linear function:

$$F_L(t) = at + b \tag{1}$$

where t is the time and a and b are the parameters being estimated. We then subtracted the fitting function equation (1) from the measured TAC in the second phase, and obtained first ($F_1(t)$) and second tracer TAC ($F_2(t)$) as

$$\begin{aligned} F_1 &= A_t(t) \quad (t < t_{2nd}) \\ &= F_L(t) \quad (t > t_{2nd}) \end{aligned} \tag{2}$$

$$\begin{aligned} F_2 &= 0 \ (t < t_{2nd}) \\ &= A_t(t) - F_L(t) \quad (t > t_{2nd}) \end{aligned} \tag{3}$$

where t_{2nd} is the time of second tracer administration. Second, the TAC of the metabolic product (recirculating water) ($F_{rw}(t)$) following $^{15}O_2$ administration was estimated in the second phase, using the modelling approach described previously (Iida *et al* 1993). The model proposed the assumption of a fixed rate constant ($k = 0.0722$ min^{-1}) for production of recirculating water, and predicted the appearance of the recirculating water from the measured whole blood TAC as

$$F_{rw}(t) = kF_2(t - \Delta t) \otimes e^{-kt} \tag{4}$$

where Δt indicates the delay time of appearance of recirculating water and $\otimes$ denotes the convolution integral. Finally, the TAC of the recirculating water (equation (4)) was added to $F_1(t)$ to obtain a TAC for $H_2^{15}O$ ($F_w(t)$), and also subtracted from $F_2(t)$ to obtain a pure TAC for $^{15}O_2$ ($F_o(t)$), i.e.,

$$\begin{aligned} F_w &= A_t(t) \quad (t < t_{2nd}) \\ &= F_L(t) + F_{rw}(t) \quad (t > t_{2nd}) \end{aligned} \tag{5}$$

$$\begin{aligned} F_o &= 0 \ (t < t_{2nd}) \\ &= A_t(t) - F_L(t) - F_{rw}(t) \quad (t > t_{2nd}). \end{aligned} \tag{6}$$

For the $^{15}O_2$–$H_2^{15}O$ protocol, we first obtained the TAC for the recirculating water due to the metabolism of oxygen during the first phase of $^{15}O_2$ administration using the modelling approach (Iida *et al* 1993) as

$$F_{rw}(t) = kA_t(t - \Delta t) \otimes e^{-kt} \quad (t < t_{2nd}) \tag{7}$$

and then separated the whole blood TAC into pure TACs for $^{15}O_2$ and $H_2^{15}O$ during the first phase. Second, we estimated the TAC for the residual radioactivity of $^{15}O_2$ during the second phase by extrapolating the estimated arterial $^{15}O_2$ TAC from the first phase by a linear function as in the case of the $H_2^{15}O$–$^{15}O_2$ protocol and then obtained pure TAC for $H_2^{15}O$ and $^{15}O_2$, i.e.,

$$\begin{aligned} F_w &= F_{rw}(t) \qquad (t < t_{2nd}) \\ &= A_t(t) - F_L(t) \quad (t > t_{2nd}) \end{aligned} \tag{8}$$

$$\begin{aligned} F_o &= A_t(t) - F_{rw}(t) \quad (t < t_{2nd}) \\ &= F_L(t) \qquad (t > t_{2nd}) \end{aligned} \tag{9}$$

where if $F_L(t)$ was less than 0, its value was set to zero.

(B) Model-based method. The input function after the injection of $H_2^{15}O$ was assumed to be the sum of two exponentials that were convolved with a Gauss function:

$$F'_w(t) = w_1 \exp(-w_3 t) \otimes g(w_5 t) + w_2 \exp(-w_4 t) \otimes g(w_6 t) \tag{10}$$

where F'_w represents the blood TAC for water administration but does not include the recirculating water from $^{15}O_2$ administration and $g(x)$ is a Gauss function as

$$g(px) = \exp(-p^2 x^2) \tag{11}$$

w_i ($i = 1$–6) are the parameters estimated.

The administration of $^{15}O_2$ is usually performed by the continuous inhalation of $^{15}O_2$ gas. The input function after the inhalation of $^{15}O_2$ was modelled using a rectangular function (f_{rect}) as follows:

$$F'_o(t) = f_{rect}(t) \otimes [o_1 \exp(-o_3 t) \otimes g(o_5 t) + o_2 \exp(-o_4 t) \otimes g(o_6 t)] \tag{12}$$

where F'_o represents the sum of the TAC of pure $^{15}O_2$ and recirculating water, and o_i ($i = 1$–6) are the parameters to be estimated. f_{rect} is defined as

$$\begin{aligned} &f_{rect}(t) = \text{constant} \quad (T_1 < t < T_2) \\ &f_{rect}(t) = 0 \qquad\quad (t < T_1 \text{ or } t > T_2) \end{aligned} \tag{13}$$

where $T_1 < t < T_2$ corresponds to the period of tracer administration.

The model function for the combined input function (F_t), i.e., whole blood TAC, is expressed by summing $F'_w(t)$ (equation (10)) and $F'_o(t)$ (equation (12)) as follows:

$$F_t(t) = F'_w(t - T_w) + F'_o(t - T_o) \tag{14}$$

where T_w and T_o denote the start time of $H_2^{15}O$ and $^{15}O_2$ administration, respectively. In our PET study, the interval between the injections of the two tracers was 180 s; therefore $T_w = 0$ and $T_o = 180$ s for the $H_2^{15}O$–$^{15}O_2$ protocol and $T_w = 180$ and $T_o = 0$ s for the $^{15}O_2$–$H_2^{15}O$ protocol.

The measured blood TAC was fitted for the whole period using the model function $F_t(t)$ in equation (14) by the variable-metric method (pseudo-Gauss–Newton method), and F'_w and F'_o were then obtained as the separated input functions. All computations, including the fitting operation, were carried out in the PAW environment (http://wwwasd.web.cern.ch/wwwasd/paw/). Finally, the TAC for recirculating water was obtained by applying the modelling approach (Iida *et al* 1993) using the obtained $F'_o(t)$ as

$$F_{rw}(t) = kF'_o(t - \Delta t) \otimes e^{-kt} \tag{15}$$

and the estimated recirculating water TAC was added to $F'_w(t)$ and subtracted from the obtained $F'_o(t)$, which resulted in the pure TACs of $H_2^{15}O$ and $^{15}O_2$, i.e.,

$$\begin{aligned} F_w(t) &= F'_w(t) + F_{rw}(t) \\ F_o(t) &= F'_o(t) - F_{rw}(t). \end{aligned} \tag{16}$$

2.2. *Simulation studies*

The reliability of the present methods was tested using actual blood TACs obtained in a series of PET studies.

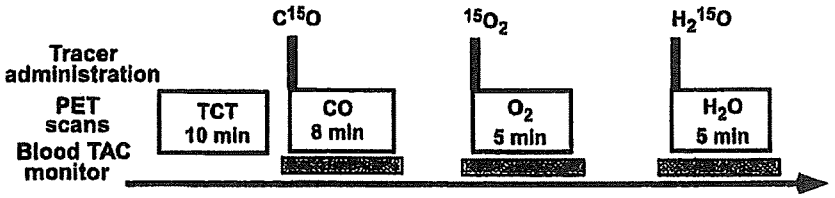

Figure 1. PET study protocol on normal human subjects. After a 10 min transmission scan and $C^{15}O$ (3000 MBq) emission scan, gaseous $^{15}O_2$ (3000 MBq) was inhaled for 1 min and a scan for 5 min was started at the same time. After sufficient time for radioactive decay of $^{15}O_2$, a $H_2^{15}O$ PET scan for 5 min was started with an intravenous administration of $H_2^{15}O$ (1110 MBq). The concentration of the radioactivity in the arterial blood was monitored (blood TAC monitor) continuously by a beta-ray detector, started at 30 s before and stopped at 30 s after the PET scan.

2.2.1. PET studies. A series of PET scans to measure the CBF and $CMRO_2$ were carried out on ten normal human subjects. All subjects were males ($n = 10$, age $= 24.6 \pm 3.3$ years, body weight $= 65.6 \pm 9.0$ kg), who provided written informed consent. The PET procedures were approved by the ethical committee of the National Cardiovascular Center. The details of the PET procedure have been described previously (Shidahara *et al* 2002). The PET scanner used was an ECAT EXACT 47 (CTI Inc., Knoxville, USA). After a 10 min transmission scan and emission scan with the administration of 3000 MBq of $C^{15}O$ for 8 min, gaseous $^{15}O_2$ of 3000 MBq was inhaled for 1 min, and a dynamic scan for 5 min was started at the same time as the inhalation. After allowing sufficient time for radioactive decay of $^{15}O_2$, another scan for 5 min was initiated with an intravenous administration of $H_2^{15}O$ into the right brachial vein. The dose was approximately 1110 MBq and the infusion period was 10 s. The study protocol is shown in figure 1.

The concentration of the radioactivity in the arterial blood was monitored continuously by means of a beta-ray detector (Kanno *et al* 1987, Iida *et al* 1986) during the PET scan. A catheter was inserted into the brachial artery, and blood was withdrawn at a flow rate of 4 ml min^{-1}. The inner diameter of the tube was approximately 1.3 mm, and the distance from the catheter to the detector was 20–25 cm. Continuous blood sampling was started at 30 s before the start of the PET scan and stopped at 30 s after the end of the scan. For each PET study, the beta-ray detector was calibrated against a NaI(Tl) well counter which was cross calibrated to the PET scanner. The calibration was carried out using $H_2^{15}O$ filled in the tube. The cross calibration factor of the detector against the well counter was from 50 to 100 cps g^{-1} cps^{-1}.

2.2.2. Simulated input function for DARG protocol and separation. Combined input function (CIF) as a simulated input function was generated by combining the experimentally obtained input functions for $H_2^{15}O$ and $^{15}O_2$ administration. Ten sets of $H_2^{15}O$ and $^{15}O_2$ arterial TACs obtained in the series of PET studies were used to generate the CIF.

It is known that the measured arterial TAC is more dispersed and delayed relative to the true input TAC in the brain, due to transverses of blood in peripheral artery and catheter tube before reaching the detector (Iida *et al* 1986, 1988, 1989, 2000, Lammertsma *et al* 1990), those terms in blood TAC were corrected. Dispersion correction (Iida *et al* 1986) was applied to the arterial blood TACs with $H_2^{15}O$ and $^{15}O_2$. Also, delay was corrected for the $H_2^{15}O$ arterial TAC (Iida *et al* 1988, Shidahara *et al* 2002) and that for $^{15}O_2$ administration was corrected by applying the same time as for $H_2^{15}O$ for the same subject. For the arterial blood TAC with $^{15}O_2$, the recirculating water was estimated using the conventional modelling approach using

equation (7) (Iida *et al* 1993). Then, sets of two input functions for pure $^{15}O_2$ and $H_2^{15}O$ were obtained, which were denoted as true input functions (TIFs). Those two blood TACs for $H_2^{15}O$ and $^{15}O_2$ were added with a time lag of 180 s of the order of $H_2^{15}O$ and $^{15}O_2$ and reverse for the $H_2^{15}O$–$^{15}O_2$ and $^{15}O_2$–$H_2^{15}O$ protocols, respectively, and the CIFs were obtained. Note that two blood TACs without the correction for the physical decay of ^{15}O were used prior to combining, and the combined curve was corrected for the physical decay of ^{15}O.

Methods (A) and (B) were applied to the CIFs to separate the $^{15}O_2$ and $H_2^{15}O$ contents. For method (A), the fitting period was selected from 80, 100, 120, 140 and 160 s to 180 s.

2.2.3. Computation of functional values. Values of CBF, OEF and $CMRO_2$ were calculated from tissue TAC ($C_i(t)$) and separated input functions for $H_2^{15}O$ ($F_w(t)$) and for $^{15}O_2$ ($F_o(t)$) using mathematical formulae, based on a single-tissue compartment model for water and oxygen (Mintun *et al* 1984). The formulae were designed to be applicable to data for tracer administration in either order $H_2^{15}O$–$^{15}O_2$ or $^{15}O_2$–$H_2^{15}O$. The total radioactivity in the tissue after $^{15}O_2$ and $H_2^{15}O$ administration can be expressed as,

$$C_i(t) = f \cdot F_w \otimes e^{\frac{-f \cdot t}{p}} + E \cdot f \cdot F_o \otimes e^{\frac{-f \cdot t}{p}} + V_B \cdot R_{Hct}(1 - F_v \cdot E)F_o(t) \tag{17}$$

where f is CBF, E is the OEF, p is a blood/brain partition coefficient for water, V_B is cerebral blood volume, R_{Hct} is the small-to-large vessel haematocrit ratio and F_v is the effective venous fraction. The first term on the right-hand side describes the amount of water entering the tissue. The second represents the amount of oxygen that enters the tissue and is immediately metabolized to water. The third expresses the radioactivity of $^{15}O_2$ in blood vessels. In the present study, we assumed that the radioactivity of $H_2^{15}O$ in the blood vessel term is negligibly small compared to the radioactivity in tissue according to the previous study (Iida *et al* 2000).

To calculate functional values using a look-up table procedure, equation (17) was integrated for the periods after $H_2^{15}O$ ($\int_w$: integrate for 90 s after rise up of $H_2^{15}O$ tissue TAC) and $^{15}O_2$ administration ($\int_o$: integrate for 180 s after rise up of $^{15}O_2$ tissue TAC) as

$$\int_w C_i(t)\,dt = \int_w (f \cdot F_w \otimes e^{\frac{-f \cdot t}{p}} + E \cdot f \cdot F_o \otimes e^{\frac{-f \cdot t}{p}} + V_B \cdot R_{Hct}(1 - F_v \cdot E)F_o(t))\,dt \tag{18}$$

$$\int_o C_i(t)\,dt = \int_o (f \cdot F_w \otimes e^{\frac{-f \cdot t}{p}} + E \cdot f \cdot F_o \otimes e^{\frac{-f \cdot t}{p}} + V_B \cdot R_{Hct}(1 - F_v \cdot E)F_o(t))\,dt. \tag{19}$$

Equation (19) can be rewritten as

$$E = \frac{\int_o (C_i(t)\,dt - f \cdot F_w \otimes e^{\frac{-f \cdot t}{p}} - V_B \cdot R_{Hct} \cdot F_o(t))\,dt}{\int_o (E \cdot f \cdot F_o \otimes e^{\frac{-f \cdot t}{p}} - V_B \cdot R_{Hct} \cdot F_v \cdot F_o(t))\,dt}. \tag{20}$$

Substituting equation (20) into (18), we obtain

$$\begin{aligned}\int_w C_i(t)\,dt = {} & \int_w (f \cdot F_w \otimes e^{\frac{-f \cdot t}{p}} + V_B \cdot R_{Hct} \cdot F_o(t))\,dt \\ & + \int_w (f \cdot F_o \otimes e^{\frac{-f \cdot t}{p}} - V_B \cdot R_{Hct} \cdot F_v \cdot F_o(t))\,dt \\ & \times \frac{\int_o (C_i(t)\,dt - f \cdot F_w \otimes e^{\frac{-f \cdot t}{p}} - V_B \cdot R_{Hct} \cdot F_o(t))\,dt}{\int_o (E \cdot f \cdot F_o \otimes e^{\frac{-f \cdot t}{p}} - V_B \cdot R_{Hct} \cdot F_v \cdot F_o(t))\,dt}.\end{aligned} \tag{21}$$

Using equation (21), f can be estimated using a look-up table procedure based on the tissue TAC and separated input functions. Next, E can be calculated using equation (20). $CMRO_2$ is

then calculated from the estimated f and E, and the measured arterial oxygen content ($[O_2]_a$) as $CMRO_2 = 1.36 \cdot [O_2]_a \cdot E \cdot f$.

2.2.4. Error analysis in the separation procedure. The error in the separation of the input function by the proposed methods propagates into the quantitative values of CBF and $CMRO_2$. This error propagation was investigated by the simulation study.

Ten sets of TIFs for $H_2^{15}O$ and $^{15}O_2$ were used to generate tissue TACs using equation (17). Two sets of physiological conditions were simulated, namely the normal condition (CBF = 50 ml/100 g min^{-1}, OEF = 0.4, CBV = 0.04 ml g^{-1}, $p = 0.8$ ml g^{-1}, $F_v = 0.835$, and $R_{Hct} = 0.85$) (Hayashi *et al* 2003) and ischaemic condition (CBF = 20 ml/100 g min^{-1}, OEF = 0.7, CBV = 0.04 ml g^{-1}, $p = 0.8$ ml g^{-1}, $F_v = 0.835$ and $R_{Hct} = 0.85$).

The combined tissue TACs for both orders of the DARG protocol, i.e. $H_2^{15}O$–$^{15}O_2$ and $^{15}O_2$–$H_2^{15}O$ were created by adding generated tissue TACs of $H_2^{15}O$ and $^{15}O_2$ with a 3 min time lag.

The values of CBF and $CMRO_2$ were calculated according to the formulae described above (equations (20) and (21)) using separated input functions from the CIF and the combined tissue TACs. The errors in the form of biases and deviations in estimated CBF and $CMRO_2$ values were calculated by comparing them with the assumed CBF and $CMRO_2$ values. These errors were presented as percentage differences between the calculated and assumed values.

2.2.5. Influence of dose of second tracer. In the DARG protocol, if administration dose of the second tracer is relatively smaller than that of the first tracer, the portion of the residual radioactivity from the first tracer in the second blood TAC becomes larger. Contrarily, if administration dose of the second tracer is larger than that of the first tracer, contribution of residual radioactivity from the first tracer on the second blood TAC becomes smaller. Therefore, errors of the separation methods and consequently the errors in the values of CBF and $CMRO_2$ might depend on the administration dose of the second tracer with respect to that of the first tracer.

We investigated how the error size would change when the second dose, i.e. the amount of the second input function, changed. For this purpose, the height of the oxygen input function in CIF was changed so that the ratio of the AUC (area under curve) between the $H_2^{15}O$ and $^{15}O_2$ input functions was changed stepwise from half to two-fold. The error size in the CBF and $CMRO_2$ values was analysed in the same way as above using separation methods (A) and (B).

2.2.6. Influence of noise in arterial TAC. The size of the error in the values of CBF and $CMRO_2$ might also depend on the statistical fluctuation in the arterial TAC, and we investigated the change in error size in the CBF and $CMRO_2$ values when the statistical fluctuations of the arterial TAC changed. To investigate the error size, 1000 noisy arterial TACs (noisy CIF) were created by adding Gaussian noise to the CIFs. The noise was added every second in a form given by $n(t) = \alpha \cdot G(\sqrt{C(t)})$. Here, $C(t)$ and $n(t)$ denote the arterial TAC count in a second without decay and noise correction at time t, respectively, and $G(\sigma)$ is the Gaussian noise with the standard deviation σ. The noise level α was defined so that the coefficient of variance in the water arterial TAC at its peak was set to 1, 2, 4, 8, 16 and 32%. The noisy arterial TACs were separated by methods (A) and (B). The values of CBF and $CMRO_2$ were then calculated using these separated TACs, and the errors in the form of biases and deviations in those values were presented as percentage differences from the assumed values. In addition, noise was also added to TIFs, and CBF, OEF and $CMRO_2$ were calculated to investigate how the noise in the

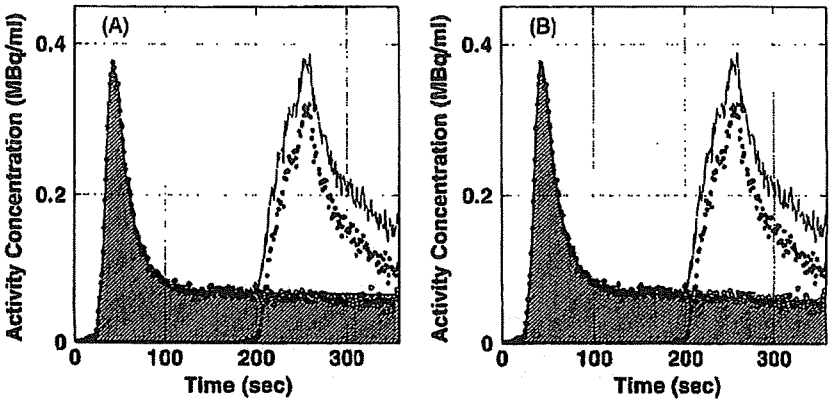

Figure 2. Estimated input function in the second phase (hatched region) from blood TAC (solid line) for DARG of $H_2^{15}O$–$^{15}O_2$. The blood TACs in which two components coexist were derived by combining two blood TACs of ^{15}O-water (white circles) and ^{15}O-oxygen (black circles) with a 180 s time lag. (A) Residual radioactivity of the first tracer was estimated by method (A) (fitting interval: 120 to 180 s). (B) Residual radioactivity of the first tracer was estimated by method (B).

arterial TAC without the separation procedure contributes to errors in the CBF, OEF and $CMRO_2$ values.

3. Results

Among ten normal subjects, the mean values of AUC for a period of 180 s for the arterial TAC were 80 ± 19 kBq ml^{-1} and 55 ± 10 kBq ml^{-1} for $H_2^{15}O$ and $^{15}O_2$, respectively. This result indicated that the values of AUC for $H_2^{15}O$ and $^{15}O_2$ had an ambiguity of approximately 20%, although all the subjects received the same amount of dose and processes for administration in the present PET study condition.

Figures 2 and 3 show examples of the separated input functions for the DARG protocols of $H_2^{15}O$–$^{15}O_2$ and $^{15}O_2$–$H_2^{15}O$ with the original and combined input functions using methods (A) and (B). It took about 40 s to separate the input function in method (B), and less than 1 s in method (A) (CPU: Intel® Pentium® D 3.2 GHz, memory: 1.0 GB, OS: Linux Fedora Core 4). For both methods and protocols, the estimated residual radioactivity in the second phase with respect to the first (hatched region) was almost identical to the true (original) input function (white circle).

For the linear method (A), the fitting interval from 120 to 180 s, where the slope of the input function became stable, provided the best fit for both the protocols, as shown in table 1. The table shows the fitting interval provided minimal bias and deviation in the difference of area under the curve between CIF and separated TAC for the residual tracer radioactivity in the second phase. When the start time of that interval was less than 120 s, the change in slope of the input function for the first tracer was large and the linear function could not reproduce the TAC of the residual radioactivity in the second phase. Further, when the time was greater, the amount of data was too inadequate to reproduce the TAC in the second phase.

Table 2 summarizes the error in the CBF and the $CMRO_2$ values due to the separation in input functions. The size of the bias and deviation in the CBF and the $CMRO_2$ values were within 4% for all separation procedures in both conditions.

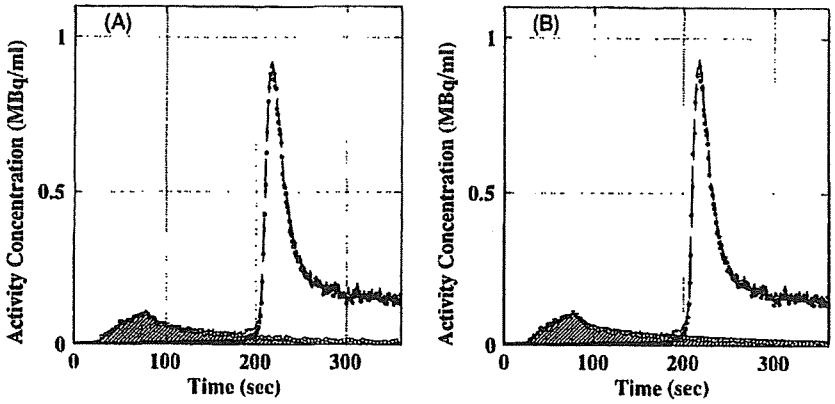

Figure 3. Estimated input function in the second phase (hatched region) from blood TAC (solid line) for DARG of $^{15}O_2$–$H_2^{15}O$. The blood TAC in which two components coexist was derived by combining two blood TACs of ^{15}O-oxygen (black circles) and ^{15}O-water (white circles) with a 180 s time lag. (A) Residual radioactivity of the first tracer was estimated by method (A) (fitting interval: 120 to 180 s) (B) Residual radioactivity of the first tracer was estimated by method (B).

Table 1. Bias and deviation in the difference of area under the curve between CIF and the estimated residual tracer radioactivity in the second phase by the linear method against the fitting interval ($n = 10$). Bias and deviation are given in %.

Fitting interval (s)	60–180	80–180	100–180	120–180	140–180	160–180
H_2O–O_2 protocol	106.9 ± 37.8	46.7 ± 44.3	10.5 ± 20.8	0.5 ± 14.5	−1.8 ± 17.2	25.4 ± 40.3
O_2–H_2O protocol	9.1 ± 5.6	8.7 ± 7.2	7.2 ± 6.6	5.3 ± 4.5	5.6 ± 7.2	7.7 ± 15.6

Table 2. Bias and deviation in CBF and $CMRO_2$ propagated from the error in the separation of $^{15}O_2$ and $H_2^{15}O$ input function ($n = 10$).

		Bias ± deviation (%)			
		Normal condition		Ischaemic condition	
Model function	Fitting interval (s)	CBF	$CMRO_2$	CBF	$CMRO_2$
$H_2^{15}O$–$^{15}O_2$					
(A)	120–180	–	−1.9 ± 4.2	–	−2.2 ± 3.5
(B)	0–360	–	0.4 ± 1.6	–	0.3 ± 1.9
$^{15}O_2$–$H_2^{15}O$					
(A)	120–180	−2.1 ± 1.2	1.3 ± 0.6	−1.7 ± 1.1	1.7 ± 0.6
(B)	0–360	−0.3 ± 1.4	0.2 ± 0.5	−0.2 ± 1.7	0.2 ± 0.1

Normal condition: CBF = 50 ml min^{-1}/100 g, OEF = 0.4; ischaemic condition: CBF = 20 ml min^{-1}/100 g, OEF = 0.7.

The bias and deviation in the value of CBF for $^{15}O_2$–$H_2^{15}O$ and $CMRO_2$ for both $H_2^{15}O$–$^{15}O_2$ and $^{15}O_2$–$H_2^{15}O$ are shown as functions of the ratio of AUC between the first and second input functions in figure 4. The size of the bias and deviation increased with the decrease in the second tracer dose and was suppressed since the second dose was increased in both methods (A) and (B). The size of the bias in the CBF by the $^{15}O_2$–$H_2^{15}O$ protocol and the $CMRO_2$ by the $H_2^{15}O$–$^{15}O_2$ protocol was 2% at most and was almost the same in the range of the AUC ratio from half to two-fold. The size of the bias in $CMRO_2$ by the $^{15}O_2$–$H_2^{15}O$ protocol was

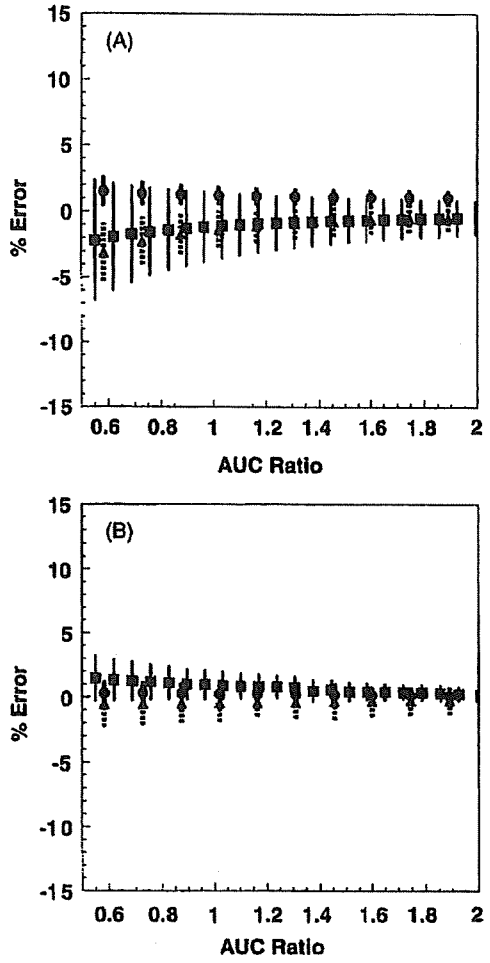

Figure 4. Error in CBF and $CMRO_2$ as a function of the dose ratio between the first to second tracer using separated input functions in method (A) (top) and (B) (bottom). The sizes of the bias in the values of CBF for $^{15}O_2$–$H_2^{15}O$ (circles) and $CMRO_2$ for $H_2^{15}O$–$^{15}O_2$ (squares) and $CMRO_2$ for $^{15}O_2$–$H_2^{15}O$ (triangles) are plotted and that of the deviation is expressed as the length of the bar.

almost negligible, and it was smaller than 0.5% in the same range of the AUC ratio. The size of the deviation for the CBF in the $^{15}O_2$–$H_2^{15}O$ protocol was less than 0.5%, and the sizes of the deviation for $CMRO_2$ in the $^{15}O_2$–$H_2^{15}O$ protocol and the $H_2^{15}O$–$^{15}O_2$ protocol were less than 3% and 4%, respectively.

The size of the bias and the deviation in the CBF, OEF and $CMRO_2$ values, due to the noise in the arterial TAC are shown in figure 5. The size of the bias for the separation method (B) (denoted by triangles) in those values was less than 5% when the noise level was less than 10%, and it was almost identical to that estimated using noisy TIF (denoted by circles). The bias by method (A) (denoted by squares) was larger than that by method (B). For the deviation with respect to the noise TIF, the size of the error in the CBF, OEF and $CMRO_2$ values was almost identical for both methods (A) and (B).

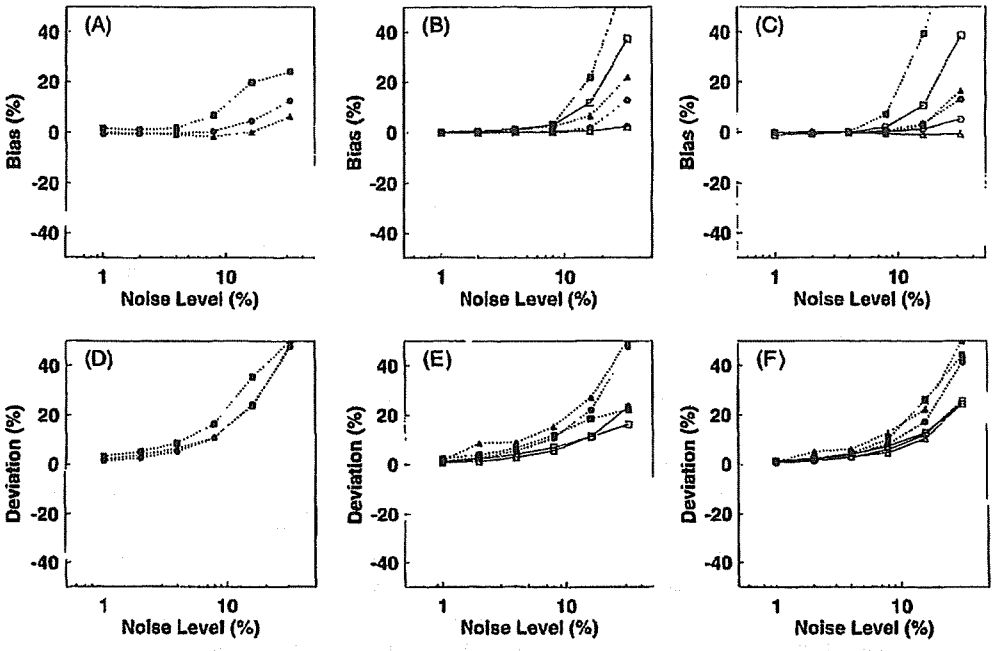

Figure 5. Bias (upper) and deviation (lower) against noise level in CBF (left), OEF (centre) and $CMRO_2$ (right) propagated from the noise on arterial TAC. The CBF, OEF and $CMRO_2$ were calculated with a noisy input function (circles) and separated input functions from the noisy arterial TAC by methods (A) (squares) and (B) (triangles), respectively. The orders of tracers $H_2^{15}O$–$^{15}O_2$ and $^{15}O_2$–$H_2^{15}O$ are indicated by white and black symbols, respectively.

4. Discussion and conclusion

We developed the separation methods of dual tracer coexistent blood TAC for the DARG protocol to avoid frequent blood sampling to calculate the quantitative CBF, OEF and $CMRO_2$ images. The present results showed that the values in CBF and $CMRO_2$ using input functions separated by the present method were reasonably accurate, i.e., the bias and deviation in CBF, OEF and $CMRO_2$ values were within 4%. When the dose of the second tracer was changed, the bias and deviation in CBF and $CMRO_2$ also changed; however, the sizes were within 5% when the ratio between AUCs in the first and second input functions was from half to two-fold. Further, the bias and deviation in the CBF and $CMRO_2$ values due to noise in the arterial TAC was less than 5% and was not severely enhanced against those from the noisy TIF.

The present results showed that the model-based function method (B) provided a more accurate value for CBF and/or $CMRO_2$ in both the $H_2^{15}O$–$^{15}O_2$ and the $^{15}O_2$–$H_2^{15}O$ protocols. The reason of the better performance of method (B) was the use of the entire period of data, although the expression of the model function was complex and the calculation took a longer time.

On the other hand, in the linear method (A), the arterial TAC was fitted with the linear function during a period of 120 to 180 s in the first phase, i.e. during the period after the shape of the first input function in the stable state, and the residual radioactivity was then estimated by extrapolating that function in the second phase. The bias and deviation in CBF and $CMRO_2$, calculated using separated input functions by method (A), were still within 4% and might be

acceptable for calculation. Thus, the present findings suggest that the dual tracer coexistent blood TAC can be separated by the linear function within a 4% accuracy. The advantages of method (A) over method (B) are easier implementation and faster computation. The linear regression program for the method (A) is readily available. On the other hand, for method (B), a computing framework for nonlinear fitting is required. We used the PAW environment for this purpose and fitting results might be different if another framework is employed. The benefit of faster computation could be minimized if a faster processor is used.

For the $^{15}O_2$–$H_2^{15}O$ protocol, the value of $CMRO_2$ was affected by the error in the separated input function, although the input function for calculating $CMRO_2$ was extracted in the first phase. This is because the $CMRO_2$ value was calculated not only from the input function and tissue TAC in the $^{15}O_2$ phase but also from the value of CBF that was estimated in the second phase and was affected by the separation error. However, the size of the error in $CMRO_2$ in $^{15}O_2$–$H_2^{15}O$ was less than 0.5% which is negligibly small. Further, the value for CBF in the $H_2^{15}O$–$^{15}O_2$ was unaffected by the error in separation, i.e., the CBF value was calculated exclusively in the first phase.

When the AUCs in the input function were almost the same between the first and second phases, the size of the bias in the value of CBF and $CMRO_2$ determined from the input function for the second phase tracer, i.e. CBF value for the $^{15}O_2$–$H_2^{15}O$ and $CMRO_2$ value for $H_2^{15}O$–$^{15}O_2$, was in the same range and was acceptable (figure 4). Moreover, the size of the bias was within a reasonable range when the ratio of the AUC between the first and second changed from half to two-fold. Practically, the present PET study on normal subjects showed that the fluctuation of the AUC of the input function was 20% when the tracer was administrated by the same procedure. This suggests that the degree of error due to the change in the ratio of the AUC of the input functions across subjects between the first and second phases could be within an acceptable range; further, the degree of error with regard to other error factors, such as delay or dispersion in input function was the same (Kudomi *et al* 2005).

Many PET scanners recently available are combined with CT scanners, and the patients reside deep inside the scanner housing during PET scanning. In this case, the length of the catheter tube must be long, which results in longer delay time and worse statistics in measured blood TAC. The size of errors as bias and deviation in CBF, OEF and $CMRO_2$ due to noise in the arterial blood TAC was less than 5% when the noise level was less than 10%. The 10% noise level corresponds to 100 cps in the measured water arterial TAC at its peak. Most devices monitoring arterial TAC can provide this level of statistics in practical examination for CBF, OEF and $CMRO_2$ evaluation for both 3SARG and DARG. Moreover, the degree of error in these values was not enhanced in comparison to that from noisy TIF. Thus, the separation procedure due to noise on the arterial TAC might not deteriorate the quantitative accuracy in CBF, OEF and $CMRO_2$.

The image quality in CBF and $CMRO_2$ by the DARG approach is influenced by the interval, relative dose, and order of the two administered tracers. Since the dose of the second tracer is less, a relatively larger amount of residual radioactivity from the first tracer remains during the image acquisition for the second tracer, and it results in the degradation of the quality of the image obtained during the second phase of the procedure. Thus, the dose of the second tracer should be as high as possible for the DARG approach in terms of the separation of the input function. However, when the dose of the second tracer is too high, the amount of random photons and dead time in the PET data would increase and the quantitative accuracy might be degraded. Further, the radiation dose increases for patients. These matters suggest that the amount and ratio of the tracer dose assumed in the present study might be appropriate for the DARG PET measurement.

The error propagation in the CBF and $CMRO_2$ values estimated in this study was based on the measured input functions obtained in the series of our PET study. The size of the error in these values might change, for example, if the $H_2^{15}O$ injection or $^{15}O_2$ inhalation period is changed. In particular, method (B) is highly dependent on the shape of the input function. Further studies are required to investigate how method (B) works when the shape of the input function is different from that of the input function we used here.

In the simulation, we used a 3 min time interval between the injections of the first and second tracers. This 3 min time interval was based on a previous simulation study (Iida *et al* 2002), which suggested that images of a quality equivalent to the 3SARG protocol could be obtained if the time interval was at least 3 min. Additionally, a 3 min scan duration for oxygen would provide reasonable image quality in CBF and $CMRO_2$ (Kudomi *et al* 2005).

In conclusion, this study demonstrates the feasibility of the separation of the dual tracer coexistent input function for rapid and simultaneous measurement of CBF and $CMRO_2$ using a single PET scan that accompanies the sequential administration of two tracers. The simulation studies showed that the present method for separation of the two components $H_2^{15}O$ and $^{15}O_2$ provides reasonable accuracy for the quantitative values of CBF, OEF and $CMRO_2$.

Acknowledgments

The authors gratefully acknowledge the staff of the Department of Nuclear Medicine, Hospital and the Department of Investigative Radiology, Research Institute, National Cardiovascular Center. The present work was supported by the Program for Promotion of Fundamental Studies in Health Science of the Organization for Pharmaceuticals and Medical Devices Agency of Japan (PMDA), by Nakatani Electronic Measuring Technology Association of Japan, and by the Program for Promotion of Fundamental Studies in Health Science of the Organization for Pharmaceutical Safety and Research (of Japan).

References

Correia J A, Alpert N M, Buxton R B and Ackerman R H 1985 Analysis of some errors in the measurement of oxygen extraction and oxygen consumption by the equilibrium inhalation method *J. Cereb. Blood Flow Metab.* **5** 591–9

Eriksson L, Holte S, Bohm C, Kesselberg M and Hovander B 1988 Automated blood sampling system for positron emission tomography *IEEE Trans. Nucl. Sci.* **35** 703–7

Eriksson L and Kanno I 1991 Blood sampling devices and measurements *Med. Prog. Technol.* **17** 249–57

Frackowiak R S, Jones T, Lenzi G L and Heather J D 1980a Regional cerebral oxygen utilization and blood flow in normal man using oxygen-15 and positron emission tomography *Acta Neurol. Scand.* **62** 336–44

Frackowiak R S, Lenzi G L, Jones T and Heather J D 1980b Quantitative measurement of regional cerebral blood flow and oxygen metabolism in man using 15O and positron emission tomography: theory, procedure, and normal values *J. Comput. Assist. Tomogr.* **4** 727–36

Fujita H, Kuwabara H, Reutens D C and Gjedde A 1999 Oxygen consumption of cerebral cortex fails to increase during continued vibrotactile stimulation *J. Cereb. Blood Flow Metab.* **19** 266–71

Hatazawa J *et al* 1995 Regional cerebral blood flow, blood volume, oxygen extraction fraction, and oxygen utilization rate in normal volunteers measured by the autoradiographic technique and the single breath inhalation method *Ann. Nucl. Med.* **9** 15–21

Hattori N, Bergsneider M, Wu H M, Glenn T C, Vespa P M, Hovda D A, Phelps M E and Huang S C 2004 Accuracy of a method using short inhalation of 15O–O2 for measuring cerebral oxygen extraction fraction with PET in healthy humans *J. Nucl. Med.* **45** 765–70

Hayashi T, Watabe H, Kudomi N, Kim K M, Enmi J, Hayashida K and Iida H 2003 A theoretical model of oxygen delivery and metabolism for physiologic interpretation of quantitative cerebral blood flow and metabolic rate of oxygen *J. Cereb. Blood Flow Metab.* **23** 1314–23

Herscovitch P, Markham J and Raichle M E 1983 Brain blood flow measured with intravenous $H_2^{15}O$: I. Theory and error analysis *J. Nucl. Med.* **24** 782–9

Ho D and Feng D 1999 Rapid algorithms for the construction of cerebral blood flow and oxygen utilization images with oxygen-15 and dynamic positron emission tomography *Comput. Methods Prog. Biomed.* **58** 99–117

Holden J E, Eriksson L, Roland P E, Stone-Elander S, Widen L and Kesselberg M 1988 Direct comparison of single-scan autoradiographic with multiple-scan least-squares fitting approaches to PET $CMRO_2$ estimation *J. Cereb. Blood Flow Metab.* **8** 671–80

Huang S C, Feng D G and Phelps M E 1986 Model dependency and estimation reliability in measurement of cerebral oxygen utilization rate with oxygen-15 and dynamic positron emission tomography *J. Cereb. Blood Flow Metab.* **6** 105–19

Iida H, Higano S, Tomura N, Shishido F, Kanno I, Miura S, Murakami M, Takahashi K, Sasaki H and Uemura K 1988 Evaluation of regional differences of tracer appearance time in cerebral tissues using [^{15}O] water and dynamic positron emission tomography *J. Cereb. Blood Flow Metab.* **8** 285–8

Iida H, Jones T and Miura S 1993 Modeling approach to eliminate the need to separate arterial plasma in oxygen-15 inhalation positron emission tomography *J. Nucl. Med.* **34** 1333–40

Iida H, Kanno I, Miura S, Murakami M, Takahashi K and Uemura K 1986 Error analysis of a quantitative cerebral blood flow measurement using H2(15)O autoradiography and positron emission tomography, with respect to the dispersion of the input function *J. Cereb. Blood Flow Metab.* **6** 536–45

Iida H, Miyake Y, Hayashi T, Kudomi N, Ogawa M, Teramoto N, Kim K M, Oku H and Hayashida K 2002 A new strategy for rapid clinical imaging of $rCMRO_2$, rCBF and rOEF using PET *J. Nucl. Med.* **43** 62P

Iida H *et al* 2000 Quantitation of regional cerebral blood flow corrected for partial volume effect using O-15 water and PET: I. Theory, error analysis, and stereologic comparison *J. Cereb. Blood Flow Metab.* **20** 1237–51

Kanno I *et al* 1987 A system for cerebral blood flow measurement using an $H_2^{15}O$ autoradiographic method and positron emission tomography *J. Cereb. Blood Flow Metab.* **7** 143–53

Kudomi N Choi C, Watabe H, Kim K M, Shidahara M, Ogawa M, Teramoto N, Sakamoto E and Iida H 2003 Development of a GSO detector assembly for a continuous blood sampling system *IEEE Trans. Nucl. Sci.* **50** 70–3

Kudomi N, Hayashi T, Teramoto N, Watabe H, Kawachi N, Ohta Y, Kim K M and Iida H 2005 Rapid quantitative measurement of $CMRO_2$ and CBF by dual administration of ^{15}O-labelled oxygen and water during a single PET scan-a validation study and error analysis in anesthetized monkeys *J. Cereb. Blood Flow Metab.* **25** 1209–24

Lammertsma A A, Cunningham V J, Deiber M P, Heather J D, Bloomfield P M, Nutt J, Frackowiak R S and Jones T 1990 Combination of dynamic and integral methods for generating reproducible functional CBF images *J. Cereb. Blood Flow Metab.* **10** 675–86

Lammertsma A A, Heather J D, Jones T, Frackowiak R S and Lenzi G L 1982 A statistical study of the steady state technique for measuring regional cerebral blood flow and oxygen utilisation using 15O *J. Comput. Assist. Tomogr.* **6** 566–73

Lammertsma A A and Jones T 1983 Correction for the presence of intravascular oxygen-15 in the steady-state technique for measuring regional oxygen extraction ratio in the brain: 1. Description of the method *J. Cereb. Blood Flow Metab.* **3** 416–24

Meyer E, Tyler J L, Thompson C J, Redies C, Diksic M and Hakim A M 1987 Estimation of cerebral oxygen utilization rate by single-bolus $^{15}O_2$ inhalation and dynamic positron emission tomography *J. Cereb. Blood Flow Metab.* **7** 403–14

Mintun M A, Raichle M E, Martin W R and Herscovitch P 1984 Brain oxygen utilization measured with O-15 radiotracers and positron emission tomography *J. Nucl. Med.* **25** 177–87

Mintun M A, Vlassenko A G, Shulman G L and Snyder A Z 2002 Time-related increase of oxygen utilization in continuously activated human visual cortex *Neuroimage* **16** 531–7

Ohta S, Meyer E, Thompson C J and Gjedde A 1992 Oxygen consumption of the living human brain measured after a single inhalation of positron emitting oxygen *J. Cereb. Blood Flow Metab.* **12** 175–92

Okazawa H, Yamauchi H, Sugimoto K, Takahashi M, Toyoda H, Kishibe Y and Shio H 2001a Quantitative comparison of the bolus and steady-state methods for measurement of cerebral perfusion and oxygen metabolism: positron emission tomography study using 15O-gas and water *J. Cereb. Blood Flow Metab.* **21** 793–803

Okazawa H, Yamauchi H, Sugimoto K, Toyoda H, Kishibe Y and Takahashi M 2001b Effects of acetazolamide on cerebral blood flow, blood volume, and oxygen metabolism: a positron emission tomography study with healthy volunteers *J. Cereb. Blood Flow Metab.* **21** 1472–9

Raichle M E, Martin W R, Herscovitch P, Mintun M A and Markham J 1983 Brain blood flow measured with intravenous $H_2^{15}O$: II. Implementation and validation *J. Nucl. Med.* **24** 790–8

Sadato N, Yonekura Y, Senda M, Iwasaki Y, Matoba N, Tamaki N, Sasayama S, Magata Y and Konishi J 1993 PET and the autoradiographic method with continuous inhalation of oxygen-15-gas: theoretical analysis and comparison with conventional steady-state methods *J. Nucl. Med.* **34** 1672–80

Shidahara M *et al* 2002 Evaluation of a commercial PET tomograph-based system for the quantitative assessment of rCBF, rOEF and rCMRO$_2$ by using sequential administration of ^{15}O-labelled compounds *Ann. Nucl. Med.* 16 317–27

Subramanyam R, Alpert N M, Hoop B Jr, Brownell G L and Taveras J M 1978 A model for regional cerebral oxygen distribution during continuous inhalation of $^{15}O_2$, C^{15}O, and C^{15}1$5O_2$ *J. Nucl. Med.* 19 48–53

Vafaee M S and Gjedde A 2000 Model of blood-brain transfer of oxygen explains nonlinear flow-metabolism coupling during stimulation of visual cortex *J. Cereb. Blood Flow Metab.* 20 747–54

Votaw J R and Shulman S D 1998 Performance evaluation of the Pico-count flow-through detector for use in cerebral blood flow PET studies *J. Nucl. Med.* 39 509–15

Original article

Nuclear Medicine Communications

Body-contour versus circular orbit acquisition in cardiac SPECT: Assessment of defect detectability with channelized Hotelling observer

Antti Sohlberg[a], Hiroshi Watabe[a], Miho Shidahara[b] and Hidehiro Iida[a]

Background The resolution of a gamma camera is depth-dependent and worsens with increasing distance to the camera resulting in a loss of fine details in SPECT images. A common approach to reduce the effects of this resolution loss is to utilize body-contour acquisition orbits. Even though body-contour orbits can improve resolution of reconstructed images their effect on lesion detection is not well known.

Objective To investigate whether body-contour orbits offer better defect detection performance than circular orbits in cardiac SPECT.

Methods The mathematical cardiac torso (MCAT) phantom was used to model ^{99m}Tc-sestamibi uptake. A total of four phantoms (two male and two female) with eight defects (four locations and two sizes) were generated and projection data were simulated using an analytical projector with attenuation, scatter, collimator response and acquisition orbit modelling. The circular and body-contour projections were reconstructed using the OSEM algorithm with/without collimator response compensation. Defect detection performance was assessed by calculating area under the receiver operating characteristic (ROC) curve for channelized Hotelling observer.

Results The defect detection performance of circular and body-contour acquisition was very similar and the difference in the area under the ROC curve between the orbits was not statistically significant with or without collimator response compensation. The collimator response compensation, on the other hand, was noticed to be valuable and it provided significantly better defect detection performance than reconstruction without it regardless of the acquisition orbit type.

Conclusions We conclude that by replacing circular orbit with more complex body-contour orbit will not lead to statistically significant increase in defect detection performance in cardiac SPECT. *Nucl Med Commun* 28:937–942 © 2007 Wolters Kluwer Health | Lippincott Williams & Wilkins.

Nuclear Medicine Communications 2007, 28:937–942

Keywords: body-contour orbit, cardiac SPECT, circular orbit

[a]National Cardiovascular Center Research Institute, Osaka, Japan and [b]Molecular Imaging Center, National Institute of Radiological Sciences, Chiba, Japan

Correspondence to Dr Antti Sohlberg, National Cardiovascular Center Research Institute, 5-7-1, Fujishiro-dai, Suita City, Osaka 565-8565, Japan
Tel: +81 6833 5012 (ext. 2559); fax: +81 6 6835 5429;
e-mail: antti@ri.ncvc.go.jp

Received 28 May 2007 Revised 31 July 2007
Accepted 31 August 2007

Introduction

The resolution of a gamma camera is depth dependent, which results in a loss of fine details in SPECT images. In order to reduce the effects of this depth dependency, body-contour acquisition orbits are often applied. Body-contour orbits improve the resolution by minimizing the object-to-detector distance and can provide approximately 1–2 mm improvement in resolution without any loss in sensitivity, when projection data is acquired with parallel hole collimators. Utilization of body-contour orbits is, however, complicated by the more complex acquisition process, especially if automatic contour tracking is used, and by the fact that body-contour orbits might be more prone to image artefacts than circular orbits [1,2]. These artefacts are generated due to resolution non-uniformity among different projections and their severity depends on the geometry of the orbit and also on orientation of the target in the field of view [3,4].

Another approach to reduce the depth-dependent blurring is to apply collimator response compensation in reconstruction. Several investigators have indicated that significant improvements in image quality can be achieved when collimator response compensation is applied during reconstruction [5–8]. Collimator response modelling might also be beneficial when combined with body-contour orbits, because in addition to its resolution enhancement capabilities collimator response correction increases uniformity of resolution and could therefore reduce the artefacts, which have been reported to reduce the quality of body-contour studies.

Image quality obtained with different acquisition and reconstruction configurations is usually assessed with traditional metrics such as resolution and contrast. Even though these metrics are easy to apply and understand they are not necessarily good predictors of defect detection performance, which is the primary concern in cardiac SPECT. In this study the channelized Hotelling observer (CHO), which has shown to correlate well with human observer performance [9], was used to compare body-contour and circular orbits with and without collimator response compensation. The goal was to determine whether body-contour orbits could offer better defect detection performance in cardiac SPECT studies than circular orbits and to find the optimal acquisition–reconstruction method combination.

Materials and methods

Phantoms

The mathematical cardiac torso (MCAT) phantom [10,11] was used to simulate ^{99m}Tc-sestamibi distribution and non-uniform attenuation in the chest region. Four different phantoms, large female/male and small female/male, were generated each with eight different defects (Fig. 1). The lateral and antero-posterior sizes were 38 cm and 26 cm for the large phantoms and 32 cm and 24 cm for the small phantoms. The relative activities per voxel assigned to myocardium, liver, kidney, spleen, lung and rest of the body were 100, 50, 100, 80, 5 and 2.5. The defects had 90° or 120° angular extent, approximately 2.5 cm length and they were simulated with 20% contrast with respect to healthy myocardium.

Projection data simulation

Noise-free projection data was simulated using an analytical projector. Attenuation was simulated with the MCAT attenuation maps and collimator response was modelled according to the method by Metz [12]. A high-resolution low-energy parallel hole collimator with 4.0 cm hole length and 0.18 cm hole radius was used in the simulations. Circular hole shape was assumed which allowed the collimator point-spread function to be calculated analytically according to:

$$g(r,D) = 2\cos^{-1}\left(\frac{|r_T|}{2R}\right) - \frac{|r_T|}{R}\sqrt{1-\frac{|r_T|^2}{4R^2}}, \quad (1)$$

where r is the distance in the detection plane from the intersection of the line perpendicular to the detection plane containing the source, D perpendicular distance from collimator to the source, R the radius of collimator hole and r_T the displacement of the centres of the projected aperture functions from the front face and back face of the collimator [13]. r_T is given by

$$r_T = r\frac{L}{D+L+C}, \quad (2)$$

where L is the collimator hole length and C the distance from back of the collimator to the detector crystal. Scatter was included using the method by Hutton [14,15]. Hutton's method consists of three steps. In the

Fig. 1

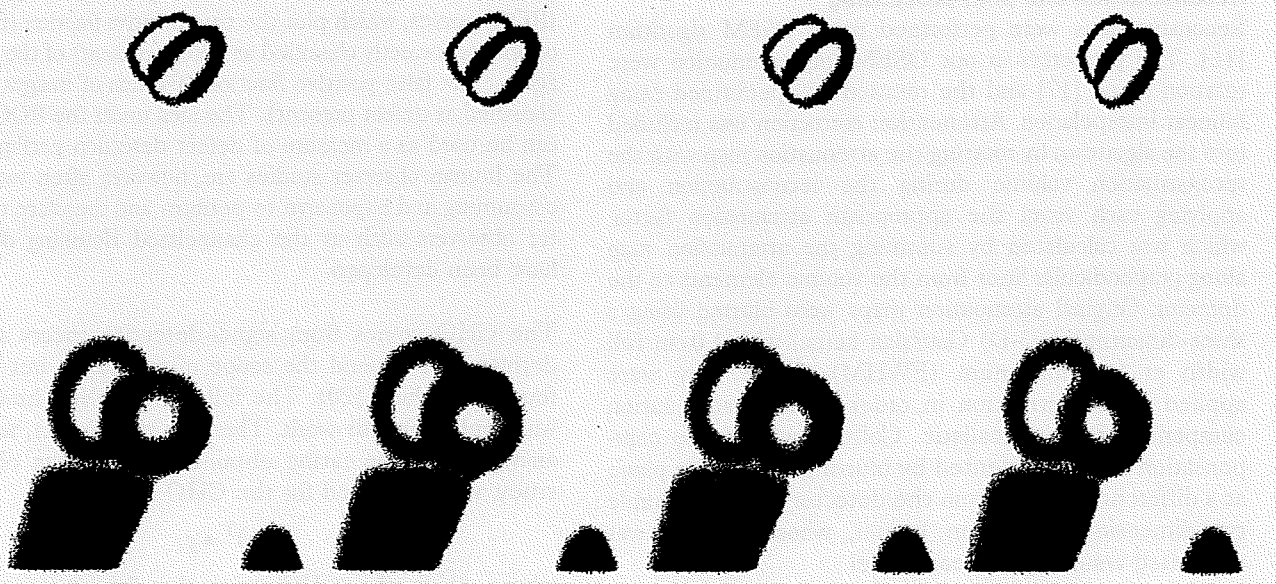

Top row: Example transverse slices of the MCAT phantoms used in the simulations. Bottom row: Example short-axis slices illustrating defect locations (defect contrast was enhanced for displaying purposes).

first step the activity distribution is convolved with monoexponential scatter kernels (exp $\alpha(d_s)r_s$), whose slopes $\alpha(d_s)$ depend on the depth in tissue (d_s). In the second step the convolved emission distribution is scaled using transmission-dependent scatter-to-true scatter fraction SF:

$$\mathrm{SF} = A - B\left(e^{-\sum_{k=j}^{k=n}\mu_k\Delta}\right)^{\gamma} - 1, \qquad (3)$$

where μ_k is the linear attenuation coefficient for voxel k, Δ the voxel size and parameters A, B and γ are fitting parameters obtained from experiment [14]. Scatter projections are finally obtained in the third step by forward projecting the convolved and scaled activity distribution at each projection angle.

Projection data was generated for 128 angles over 360° arc using 256 × 256 projection matrix and 0.156 cm pixel size. The radius of rotation for the body-contour orbits, at each projection angle, was determined by tracking the distance from the centre of rotation to the surface of the attenuation map of each four phantoms and circular orbit's radius of rotation was set to the maximum radius found in the corresponding body-contour orbit study. After simulation the projections were collapsed into 64 × 64 matrix size and Poisson noise was added. Projections were scaled so that the number of total counts was approximately 3.0 MCts. A total of 480 noisy projection data sets (four phantoms × eight defects × 15 noise realizations) with defect and 480 projection data sets (four phantoms × 120 noise realizations) without defect were generated for both orbits.

Reconstruction and post-processing

Reconstructions were performed using OSEM algorithm [16]. The projectors in our OSEM implementation were rotation based [17] and the rotation was performed using bilinear interpolation. Attenuation correction was included into the algorithm by rotating the attenuation map with the reconstruction volume during the reconstruction and applying each voxel the appropriate attenuation factor, which was calculated by summing the attenuation map along perpendicular lines from the volume elements to the detector. Original attenuation maps were blurred using a three-dimensional (3-D) Gaussian kernel with 1.0 cm full width at half maximum (FWHM) before they were applied in reconstruction in order to make attenuation compensation more realistic. Collimator response compensation was implemented by blurring each image plane at a different distance from the detector with a separable two-dimensional Gaussian kernel, whose FWHM was calculated assuming a linear model

$$\mathrm{FWHM}(D) = \alpha + \beta D, \qquad (4)$$

for the decrease of resolution as a function of distance (D) from the detector. The α and β parameters were obtained by simulating point sources at different distance from the collimator using the analytic projector described in previous section. FWHMs of these measurements were calculated and the linear model in Equation 4 was fitted to the measurements. It is worthwhile to note that collimator response compensation was performed using a different method that was used to simulate the projection data. This approach should provide more realistic results with collimator correction, which are not 'too good' due to the complete match of the projectors used in generation of the projection data and reconstruction. Correction for scatter was not performed.

Every noisy circular and body-contour projection data set was reconstructed with/without collimator response compensation using 32 subsets and two iterations. Reconstructed images were post-filtered with 3-D Gaussian filter with 1.25 cm FWHM. These reconstruction/post-filtering parameters have shown to provide near optimal defect detection performance in previous studies [18,19]. After filtering, images were realigned into short-axis slices and a single slice through the centre of the defect (for defect absent images the corresponding slice) was extracted for further analysis.

Channelized Hotelling observer and receiver operating characteristic analysis

Defect detection performance is most often measured using human observers. In these studies observers are shown a large number of images with and without defects acquired/reconstructed using the methods, which are to be compared against each other. The observers rate the existence of a defect, e.g., with a continuous scale from 0 (defect definitely absent) to 100 (defect definitely present). These ratings are then used to generate a receiver operating characteristic (ROC) curves, which plot the true positive fraction (fraction of images correctly classified as defect present) of the ratings against the false positive fraction (fraction of images falsely classified as defect present). The area under the ROC curve can be used as a measure of defect detection performance. The human observer studies are, however, often too time-consuming and expensive to perform and therefore computer observers such as the channelized Hotelling observer have been developed.

The CHO comes from signal-detection theory and its derivation is beyond the scope of this paper, but can be found elsewhere [20]. The following explains how CHO was applied in this work. The test statistic (λ), which is analogous to the rating obtained in a human observer study, was calculated for the CHO as

$$\lambda = h^{\mathrm{T}} \bullet g, \qquad (5)$$

where h^{T} is the CHO, g is the feature vector and superscript T denotes transpose operation. The feature vector was obtained by processing the short-axis slice under testing by frequency selective channels, which

have been added to computer observers to mimic human visual processing of images [18]. In this study four rotationally symmetric channels with 1/64–2/64, 2/64–4/64, 4/64–8/64 and 8/64–16/64 cycles/pixel passbands were used. The frequency channels were shifted to each defect centre (shift was performed also for defect absent images) with a phase shift and the channels were converted into spatial domain with inverse Fourier transform. The CHO was calculated as

$$h^{T} = (\langle g_1 \rangle - \langle g_2 \rangle)^{T} S_{II}^{-1}, \quad (6)$$

where $\langle g_1 \rangle$ is the mean feature vector for defect present images, $\langle g_2 \rangle$, mean feature vector for defect absent images and S_{II} the intraclass scatter matrix [18,21]. First half of the short axis slices for each orbit/reconstruction method combination were used to calculate the CHO and the remaining half of the images were used to obtain the actual test statistics. Each receiver operating characteristic (ROC) curve was therefore estimated from the rating data of 240 defects present (four phantoms × eight defects × 15 noise realizations ÷ 2) and 240 defect absent (four phantoms × 120 noise realizations ÷ 2) images. The ROC curves and areas under the curves (AUC) were obtained using the ROCKIT software (http://www-radiology.uchicago.edu/krl).

Results

The results of the acquisition orbit comparison are presented in Table 1 and Fig. 2. As can be seen body-contour orbit offers slightly better defect detection performance than circular orbit when collimator response compensation is not applied, but the difference in the AUC values between the two orbits is not statistically significant at $P = 0.05$ level. Interestingly circular orbit performs better with collimator response correction than body-contour acquisition. This is probably due to the fact that the reconstruction voxel size is quite large compared to the FWHM of the Gaussian that is used to model the collimator response, which might lead to relatively crude presentation of the blurring kernels. With body-contour orbits this phenomenon has even bigger effect, because the imaging distance is shorter and thus the Gaussian kernels are narrower. It is, however, important to note that the difference in AUCs between circular and body-contour orbits when collimator response compensation is applied is not statistically significant.

Table 1 Comparison between circular/body-contour acquisition and reconstruction with/without collimator response compensation (coll)

Method 1	Method 2	AUC 1	AUC 2	P
Circular w/o coll	Contour w/o coll	0.856	0.862	0.358
Circular w coll	Contour w coll	0.901	0.894	0.325
Circular w/o coll	Circular w coll	0.856	0.901	<0.001
Contour w/o coll	Contour w coll	0.862	0.894	<0.001

Fig. 2

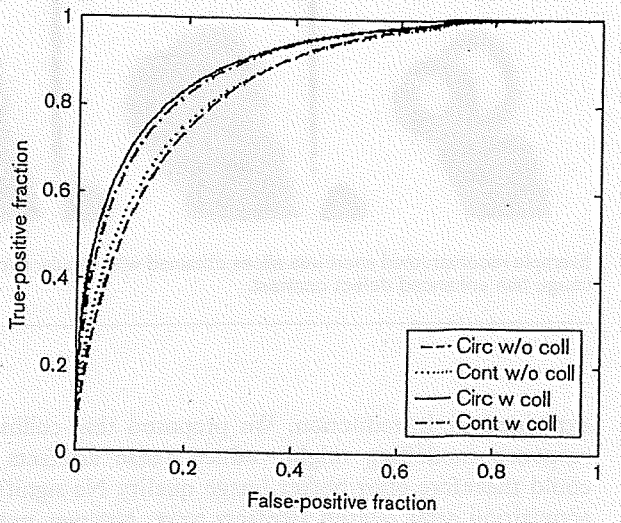

ROC curves for circular and body-contour orbit studies reconstructed with/without collimator response compensation (coll).

Figure 3 shows representative images from circular and body-contour orbit studies. When comparing individual images it is worthwhile keeping in mind that circular and body-contour images correspond to different projection data noise realizations and thus some of the differences seen in images might be due to noise and not different acquisition orbits. Overall there are no large differences among the images. Reconstructions with collimator response compensation provide smoother and thus perhaps more visually pleasing image quality than reconstruction without correction.

Discussion

Body-contour acquisition orbits have the ability to increase resolution and contrast, but their effect on defect detection performance in cardiac SPECT is not well known. This study compared circular and body-contour orbits using CHO and ROC analysis. The defect detectability with the two orbits was noticed to be quite similar. The difference in areas under the ROC curve was 0.006 for reconstruction without collimator modelling and 0.007 with collimator modelling. Even though the body-contour orbit increased the area under curve, when collimator response correction was not applied, it could not provide statistically significant improvement in defect detection performance. Similar findings were made by White *et al.* [22], who reported that circular and body-contour orbits do not differ significantly in terms of defect extent, reversibility or size assessment.

Body-contouring adds extra complexity to acquisition procedure and may generate additional artefacts as